Embryogenesis of the peristaltic reflex

Nicolas R. Chevalier[1] (iD), Nicolas Dacher[1], Cécile Jacques[1], Lucas Langlois[1], Chloé Guedj[2] and Orestis Faklaris[2,3]

[1]*Laboratoire Matière et Systèmes Complexes, Université Paris Diderot/CNRS UMR 7057, Sorbonne Paris Cité, 10 rue Alice Domon et Léonie Duquet, 75013 Paris, France*
[2]*Imagoseine Core Facility, Institut Jacques Monod, Université Paris Diderot/CNRS UMR7592, 15 rue Hélène Brion, 75013 Paris, France*
[3]*MRI Core facility, Biocampus, UMS 3426 CNRS – Université Montpellier, 141 rue de la Cardonille, 34094 Montpellier Cedex 5, France*
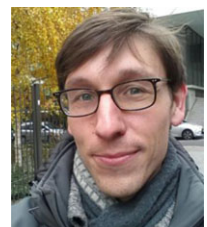
Edited by: Kim Barrett & David Grundy

The Journal of Physiology

Key points

- Neurogenic gut movements start after longitudinal smooth muscle differentiation in three species (mouse, zebrafish, chicken), and at E16 in the chicken embryo.
- The first activity of the chicken enteric nervous system is dominated by inhibitory neurons.
- The embryonic enteric nervous system electromechanically couples circular and longitudinal spontaneous myogenic contractions, thereby producing a new, rostro-caudally directed bolus transport pattern: the migrating motor complex.
- The response of the embryonic gut to mechanical stimulation evolves from a symmetric, myogenic response at E12, to a neurally mediated, polarized, descending inhibitory, 'law of the intestine'-like response at E16.
- High resolution, whole-mount 3D reconstructions are presented of the enteric nervous system of the chicken embryo at the neural-control stage E16 with the iDISCO+ tissue clarification technique.

Abstract Gut motility is a complex transport phenomenon involving smooth muscle, enteric neurons, glia and interstitial cells of Cajal. Because these different cells differentiate and become active at different times during embryo development, studying the ontogenesis of motility offers a unique opportunity to 'time-reverse-engineer' the peristaltic reflex. Working on chicken embryo intestinal explants *in vitro*, we found by spatio-temporal mapping and signal processing of diameter and position changes that motility follows a characteristic sequence of increasing complexity: (1) myogenic circular smooth muscle contractions from E6 to E12 that propagate as waves along the intestine, (2) overlapping and independent, myogenic, low-frequency, bulk longitudinal smooth muscle contractions around E14, and (3) tetrodotoxin-sensitive coupling of longitudinal and circular contractions by the enteric nervous system as from E16. Inhibition of nitric oxide synthase neurons shows that the coupling consists in nitric oxide-mediated relaxation of circular smooth muscle when the longitudinal muscle layer is contracted. This mechano-sensitive coupling gives rise to a directional, cyclical, propagating bolus transport pattern: the migrating motor complex. We further reveal a transition to a polarized, descending, inhibitory

---

---

reflex response to mechanical stimulation after neuronal activity sets in at E16. This asymmetric response is the elementary mechanism responsible for peristaltic transport. We finally present unique high-resolution 3D reconstructions of the chicken enteric nervous system at the neural-control stage based on confocal imaging of iDISCO+ clarified tissues. Our study shows that the enteric nervous system gives rise to new peristaltic transport patterns during development by coupling spontaneous circular and longitudinal smooth muscle contraction waves.

Corresponding author N. R. Chevalier: Laboratoire Matière et Systèmes Complexes, Université Paris Diderot/CNRS UMR 7057, Sorbonne Paris Cité, 10 rue Alice Domon et Léonie Duquet, 75013 Paris, France. E-mail: nicolas.chevalier@univ-paris-diderot.fr

Introduction

The gut is a very sophisticated, autonomous, mechano-chemical reactor. Synchronized movements of muscles within the gut wall, collectively termed motility, permit the transport, mixing and absorption of the food bolus. Speaking in engineering terms, the specifications that the gut as an engine must comply with are substantial. It must actively propel a food bolus with variable rheological properties (from liquid to solid) and adjust the speed of propulsion and local flow in the vicinity of the gut epithelium to ensure optimal absorption of nutrients. Any residual content has to be expelled to prevent stasis and infection. Facing microbial or viral stress, it must be able to flush gut contents at high speed (diarrhoea) or on the contrary switch to vomiting, if necessary. Accomplishing all these tasks obviously requires two-way feedback between the digestive 'chemical' (epithelium and mucosa) and 'mechanical' (longitudinal and circular smooth muscle) compartments of the gut. The need for mechano-chemical crosstalk is the *raison d'être* of the enteric nervous system (ENS), an intrinsic nervous control system that is unique among smooth muscle-lined organs (e.g. blood vessels, ureter, oviduct). The anatomical subdivision of the ENS into interconnected myenteric, smooth muscle-innervating and submucous, epithelium-innervating plexuses reflects the dual mechano-chemical interfacing role of this nerve network (Hu & Spencer, 2018).

Physiological studies of motility have revealed a panoply of contractile regimes (http://humanbiology.wzw.tum.de; Spencer *et al.* 2016): colonic migrating motor complexes, peristalsis, segmentation, myogenic ripples and slow waves. Studies on isolated adult gut segments in organ baths have aimed at grasping the chemical and mechanical factors underpinning these movements, in order to reduce the apparent variety and complexity of movements observed to a minimal number of elementary, local behavioural laws. Although incredible strides (Spencer *et al.* 2016) have been made in this pursuit since the pioneering studies of Bayliss and Starling (1899), this approach has also been challenged by the shear complexity of the adult gut. More than 30 functional types of neurons are present in the ENS synthesizing about 25 different neurochemicals, although only a very small number actually meet the criteria to be considered neurotransmitters (McConalogue & Furness, 1994). This makes it necessary to apply an arsenal of pharmacological agents (Daniel *et al.* 1989) that often present concentration-dependent effects. Motility patterns and contractile behaviour depend on the gut segment location (duodenum, hindgut, etc.), on animal species (guinea-pig, mouse, etc.) and on the preparation method (open, tubular, muscle strips, etc.). Common apparatus used to measure smooth muscle contractility was recently found to interfere with the physiological motility pattern (Barnes *et al.* 2014).

In the face of this complexity, the approach we adopt and expand upon here is to deconstruct ('reverse-engineer') adult motility by examining how it develops in the embryo. The first motility patterns in the embryonic mouse (Roberts *et al.* 2010), zebrafish (Holmberg *et al.* 2007) and chick (Chevalier *et al.* 2017) have all been shown to be myogenic, i.e. they are insensitive to neuronal inhibitors, and are present in gut tissue devoid of enteric nervous system (Roberts *et al.* 2010; Chevalier *et al.* 2017) or of interstitial cells of Cajal (Roberts *et al.* 2010). We have recently demonstrated that early digestive movements are underpinned by calcium waves that travel through a circular smooth muscle syncytium (Chevalier, 2018). All attributes of early motility are virtually identical to those of calcium waves: constant speed propagation without attenuation, counter-propagating wave annihilation, and sensitivity of wave generation to mechanical stimulation or wounding. The first detectable neuronal subtypes are predominantly inhibitory (Hao & Young, 2009); calcium activity of neurons can be detected in mice around E12.5 (Hao *et al.* 2013, 2017), i.e. preceding their first detectable influence on motility patterns. The first neurally controlled movements emerge at E18.5 in the mouse duodenum in the form of a tetrodotoxin (TTX)-sensitive migrating motor complex (MMC; Roberts *et al.* 2010). In the zebrafish, motility was found to be TTX-sensitive at 7 days post-fertilization (Holmberg *et al.* 2007). The lack of enteric nerves in the dysfunctional

colon of Hirschsprung disease patients is a testimony to the essential role of the ENS in adult gut motility (Ro *et al.* 2006; Roberts *et al.* 2008).

The investigations we report on here were initially motivated by the empirical observation that, in all species examined, onset of neurally controlled motility occurs shortly after longitudinal smooth muscle differentiation (E16.5 in mice (Walton *et al.* 2016), days 4–5 in zebrafish (Wallace *et al.* 2005)). Several studies on adult motility indicate that the myenteric nerve plexus plays an essential role in synchronizing calcium activity between longitudinal and circular muscle layers (Stevens *et al.* 2000; Spencer *et al.* 2007). We were therefore keen on firstly detecting the onset of longitudinal contractile movements in the gut after differentiation of this smooth muscle layer, and secondly examining how the emergence of neurally controlled movements relates to the activity of both circular and longitudinal muscle layers. We resorted to simple, contactless imaging of gut kinematics in minimalistic tubular preparations to avoid mechanical interference with the samples (Barnes *et al.* 2014). The main conclusion of our study is that the enteric nervous system generates new motility patterns by coordinating spontaneous, myogenic, circular and longitudinal smooth muscle contractions. The mechanosensitive coupling consists in nitric oxide (NO)-mediated, caudally polarized relaxation of the circular muscle layer when the ENS is distended, i.e. when longitudinal muscle is contracted, when bolus is present or when the gut is pinched. We conclude by presenting unique high-resolution 3D reconstructions of the chicken enteric nervous system at the neural-control stage E16 based on confocal imaging of iDISCO+ clarified tissues.

Methods

Ethics

The experiments were conducted under European law article 2016/63/UE: the approval of experimental protocols by an ethics committee is not required for research conducted on chicken at embryonic stages. All experiments were performed in accordance with the ethics guidelines of CNRS. Animal pain was minimized by rapid decapitation immediately after the eggs were cracked open. The investigators understand the ethical principles under which *The Journal of Physiology* operates and certify that their work complies with its animal ethics checklist.

Specimen preparation

Fertilized chicken eggs were purchased from EARL Morizeau (Chartres, France, breeder Hubbard, JA57 hen, I66 rooster, yielding type 657 chicks). The total number of embryos reported on in this work is ∼95. The eggs were incubated at 37.5 °C in a humidified chamber for 12–16 days. The gastrointestinal tracts were dissected from hindgut to stomach, the mesentery and Remak's nerve were removed. Duodenum (just after the stomach), jejunum (just before the umbilicus) and hindgut segments (∼1 cm) were collected.

Motility observation set-up, drugs and mechanical stimulation

The experimental set-up is described in Fig. 1*A*. Opened or tubular gut segments were pinned at their extremities, in a vertical position, to the wall of a rectangular trough coated with Sylgard. The trough was filled with 40 mL DMEM GlutaMAX^{TM}-I (Thermo Fisher Scientific, France; with 4.5 g/L D-glucose and sodium pyruvate, Ca^{2+} 1.8 mM, Mg^{2+} 0.8 mM), covered and heated from below with a heating plate to a temperature of 36.5 ± 1°C. The medium was constantly bubbled with carbogen (95% O_2–5% CO_2); rising bubbles generated a flow in the trough that replenished oxygen in the vicinity of the explants.

We waited 30 min after the guts were introduced in the trough to stabilize temperature and oxygen levels. This method yielded stationary motility patterns for the duration of the experiment (1–2 h). Oxygenating by passive O_2 diffusion through a thin meniscus of medium as we previously described for early stage guts (E5–E9) (Chevalier *et al.* 2017) is not satisfactory at late development stages (E12+) as the thickness of the tissue and its oxygen demand increase. The contractile activity 30 min before and 30 min after drug addition to the medium was then recorded by time-lapse imaging (0.5–3 Hz) with a video camera. In most experiments five segments were recorded simultaneously, up to eight for stage E12 guts. Drugs applied include: tetrodotoxin (TTX; 1 μM; Abcam, Cambridge, UK; ab120055), N^{ω}-nitro-L-arginine (NOLA; 100 μM; Santa Cruz Biotechnology sc-3570), sodium nitroprusside (SNP; 100 μM; Sigma-Aldrich 71778), atropine sulfate (10 μM; Sigma-Aldrich A0257). All drugs were prepared as 100× or 1000× stock solutions in distilled water; NOLA, SNP and atropine stock solutions were prepared fresh before each experiment. To mechanically stimulate (pinch) the guts, we pulled a Pasteur pipette to a diameter of ∼200–500 μm and blunted its end with a flame to prevent damage to the gut tissue. The pressure was applied for ∼1 s and caused a ∼20–50% diameter increase of the gut in the direction perpendicular to the applied force. We waited 2–4 min between each pinch and continuously recorded the contractile response of the guts.

Motility analysis

Our analysis method is described in Fig. 1*B–E*. Image stacks were analysed with ImageJ. The Reslice function

was applied to a region-of-interest (ROI) along the gut (long vertical dashed rectangle in Fig. 1*B*) to generate spatiotemporal maps (Fig. 1*C*). These maps are similar to D-maps (Lentle & Hulls, 2018), but the grey level is not directly proportional to the diameter change. The rostro-caudal axis runs from top to bottom for all maps shown. Circular contraction waves appeared as slanted lines (arrowheads, Fig. 1*C*); the average angle α (Fig. 1*C*) of five circular contractions was measured to calculate their speed $v = 1/\tan\alpha$. The Reslice function was applied to a ROI perpendicular to the gut (small transverse dashed rectangle in Fig. 1*B*). A threshold was applied to the resulting image and further analysed with MATLAB (The MathWorks Inc., Natick, MA, USA) software to extract the local diameter $d(t)$ (distance between left and right edges) and local x position $p(t)$ (average of left and right edges) of the segment. The y position of the ROI was chosen in such a way that the gut was locally always perpendicular to the ROI, even when it rocked to the side. The signal $d(t)$ exhibited high frequency ~ 3 cycles per minute (cpm) oscillations (Fig. 1*D*, blue line) resulting from circular contraction waves; we Fourier

transformed this signal (Fig. 1*D*, right) to extract the circular contraction frequency. Using MATLAB signal processing routines, we further extracted the upper $d_+(t)$ and lower $d_-(t)$ envelope of the diameter (Fig. 1*D*), as well as the averaged, smoothed diameter $d_s(t)$ (Fig. 1*D*); the instantaneous circular contraction amplitude was defined as $A_c(t) = (d_+(t) - d_-(t))/d_s(t)$. This is an amplitude of diameter fluctuations induced by the contractions, not of muscle tension or of depolarization. The signal $p(t)$ exhibited low frequency ~ 0.3 cpm oscillations (Fig. 1*E*) that we identified (see Results) as resulting from longitudinal contractions, and that were also visible as a low-frequency signal on spatiotemporal maps (white arrows, Fig. 1*C*). Position extremes coincided with diameter extremes (see dashed lines connecting Fig. 1*D* and Fig. 1*E*) because $d_s(t)$ was maximal when the longitudinal muscle was contracted and vice versa. We Fourier transformed the smoothed $p(t)$ (Fig. 1*E*, right) to extract the longitudinal contraction frequency.

In E16 duodenum, we noticed that when longitudinal muscle was contracted ($d_s(t)$ peaks, see Fig. 2*C*), $A_c(t)$ significantly decreased, i.e. these two signals were out of
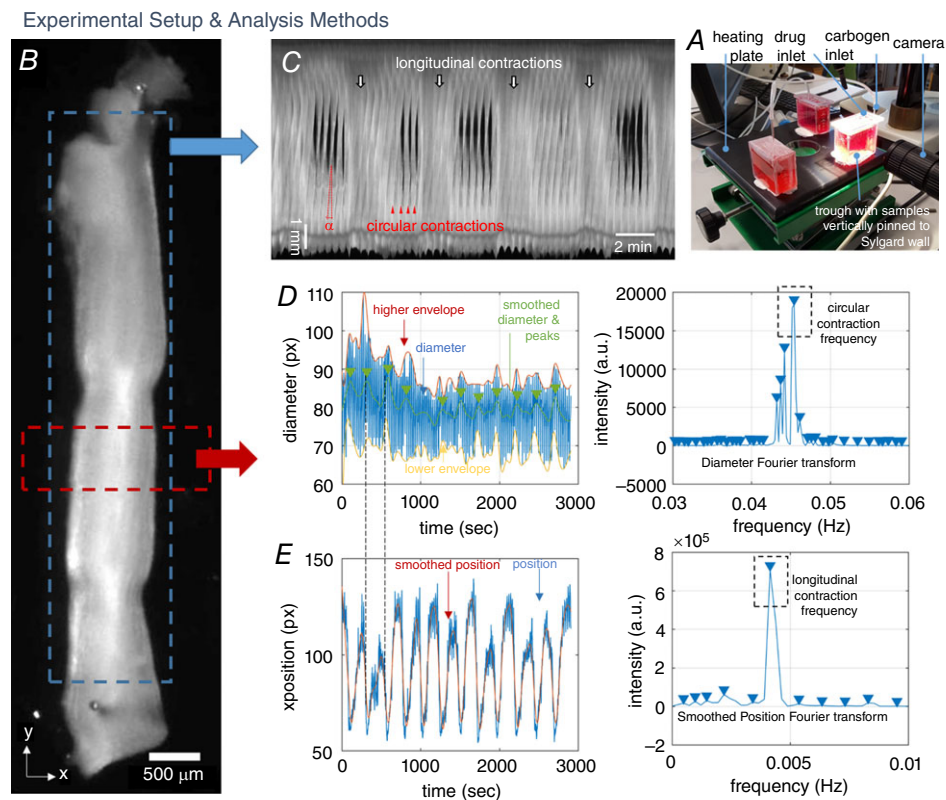
Figure 1. Experimental and analytical methods
A, photograph of the motility monitoring setup. *B*, still shot of tubular E16 jejunum segment. Dashed rectangles are longitudinal and transverse regions-of-interest used to generate the data in *C* and in *D–E*, respectively. *C*, spatiotemporal map ('diameter-type map' or 'D-map'). *D*, left: diameter *vs.* time plot $d(t)$ and signal processing. Right, Fourier transform of $d(t)$. *E*, left: *x*-position *vs.* time plot $p(t)$. Right, Fourier transform of $p(t)$ showing longitudinal contraction frequency.
[Colour figure can be viewed at wileyonlinelibrary.com]

phase. To quantify this interplay, we computed the Pearson correlation coefficient

$$\rho(d_s, A_c) = \frac{-1}{T-1} \sum_{t=1}^{T} \left(\frac{d_s(t) - \mu_{d_s}}{\sigma_{d_s}} \right) \left(\frac{A_c(t) - \mu_{A_c}}{\sigma_{A_c}} \right)$$

with the MATLAB corrcoeff() function, where T is the total time of a recording period, μ_{d_s} and σ_{d_s} are the mean and standard deviation of d_s, and μ_{A_c} and σ_{A_c} the mean and standard deviation of A_c. ρ values are between -1 and 1; completely correlated (in-phase) and anti-correlated (out-of-phase) signals have, with this definition (notice the minus sign), respectively, a ρ of -1 and 1. As a further measure of correlation, we computed the time-averaged $A_c(t)$ in a window of ± 10 s around all diameter valleys (minima) $A_{c,\text{valleys}}$ and around all diameter peaks (maxima) $A_{c,\text{peaks}}$, and calculated the valley–peak contractile amplitude difference as VP $= A_{c,\text{valleys}} - A_{c,\text{peaks}}$. Because amplitude is stronger at diameter valleys than at diameter peaks for E16 duodenums, we found VP > 0 in most of these samples.

We time-averaged $A(t)$ and $d_s(t)$ in the 500 s before and after drug addition, respectively, to get the averaged circular contraction amplitude and averaged smoothed diameter just before and right after drug addition. We did not average these quantities over the whole recording period because they presented a slow drift in time that was independent of the drug and that occurred even after a prolonged equilibration period; the diameter tended to become gradually smaller and the amplitude gradually
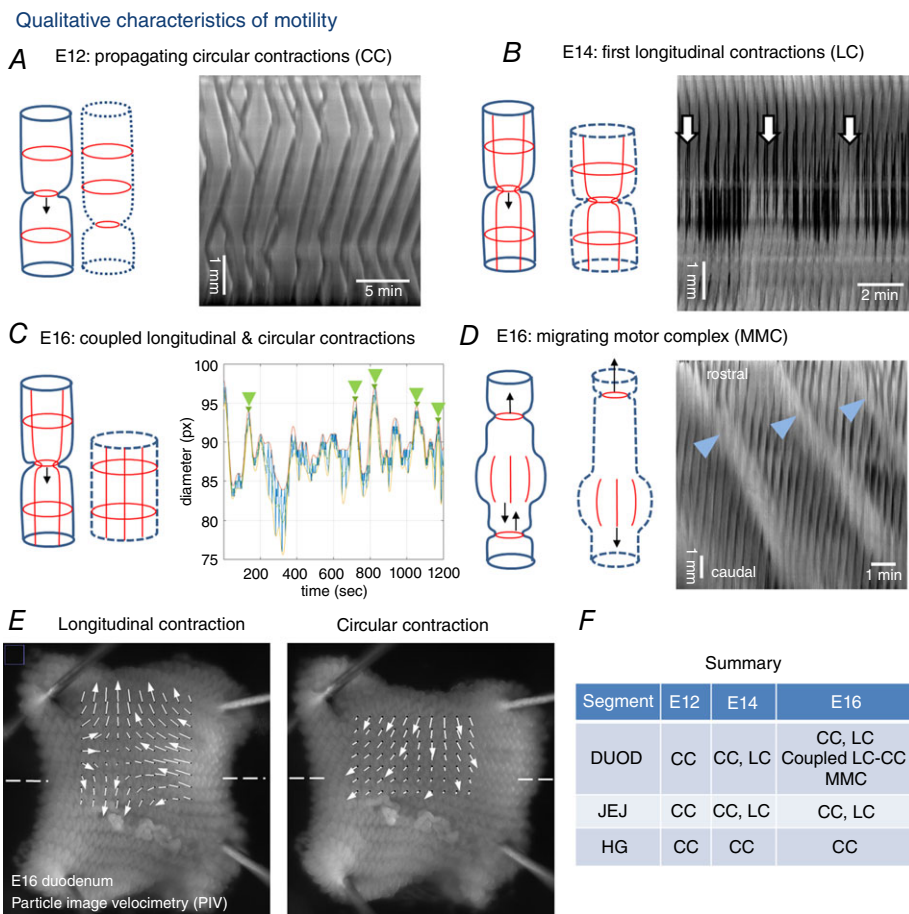
Figure 2. Motility patterns and characteristics from E12 to E16
A–D, schemes of motility patterns. Full and dashed contours indicate the state of the gut at *t* and *t* + Δ*t*, to portray its dynamics. Thin lines indicate the smooth muscle fibre orientation and contractions. Spatiotemporal diagrams or diameter–time plots illustrate the emerging features at each stage. White arrows in *B* and green arrowheads in *C*: longitudinal contractions. Blue arrowheads in *D*: propagating contraction complexes. *E*, still shots (Video S1) of open preparations of E16 duodenum, the epithelium faces the reader. Dashed white line: long axis of the gut. The vectors indicate the displacement of features of the epithelium between two frames (1 s interval) during a longitudinal contraction (left) and during a circular contraction (right). *F*, summary of movements observed in the duodenum (DUOD), jejunum (JEJ) and hindgut (HG) at stages E12–E16. CC, circular contraction; LC, longitudinal contraction; MMC, migrating motor complex.
[Colour figure can be viewed at wileyonlinelibrary.com]

higher, most likely because of viscous deformation of the gut under the effect of repeated circular contractions. All other quantities were computed from the whole 30 min recording period before and after drug addition.

We emphasize that we did not measure the mechanical tension developed by the muscle layers. We measured circular muscle activity by assessing the local diameter reduction it induces (distinctly seen on spatiotemporal maps and supplementary videos) when this layer is contracted. We measured longitudinal muscle activity by the periodic transverse displacement of the pinned segments (buckling) caused by these changes in length. Due to passive, purely mechanical cross-effects, circular muscle contraction causes some degree of elongation, and conversely, longitudinal muscle contraction induces some distension. In tubular preparations in a stationary physiological state, these passive cross-effects are relatively small compared to the main deformations induced by circular and longitudinal contractions. Longitudinal and circular motions have highly distinct intrinsic frequencies (0.3 and 3 cpm respectively) in the chicken embryonic gut, so that the two can be very clearly distinguished and any potential artifact from passive mechanical cross-effects discarded, as clearly seen in Supporting information Videos S1 and S3–S6. Passive effects can be seen on longer time scales (~hours) because the tissue is viscoelastic, or upon applying drugs that abruptly change muscle tone (like TTX on E16 duodenum, see Results).

Sample clearing and whole-mount 3D Tuj and DAPI confocal imaging

In brief, samples were dehydrated, bleached, immuno-stained and clarified according to a modified iDISCO+ clearing protocol (Renier *et al.* 2016; Belle *et al.* 2017). Samples were dehydrated for 1 h at room temperature (RT) in ascending concentrations of methanol (50%, 80%, 100%) in phosphate-buffered saline (PBS), left overnight at 4°C in a 6% hydrogen peroxide solution in 100% methanol for bleaching, re-hydrated on the following day in descending concentrations of methanol (100%, 80%, 50%) and washed in PBS. Samples were permeabilized and blocked in PBS containing 0.2% gelatin (BDH-Prolabo, VWR, Stockholm, Sweden) and 0.5% Triton X-100 (Sigma-Aldrich) (PBSGT) at RT on a rotating tray. Immunostaining for Tuj anti-βIII-tubulin (Abcam, 14545, dilution 1:100) was performed in 0.1% saponin (10 μg/mL) in PBSGT at RT with agitation for 3 days, followed by six washes of 30 min in PBSGT at RT. Secondary antibodies (Cy3 or green fluorescent protein (GFP), dilution 1:300) applied in 0.1% saponin (10 μg/mL) in PBSGT at RT for 2 days. After staining samples were exposed to a 4′,6-diamidino-2-phenylindole (DAPI) solution for 6 h and protected from light by covering in aluminium foil. For clearing we followed

the iDISCO+ protocol (Renier *et al.* 2016): samples were dehydrated in a series of methanol in PBS solutions (20%, 40%, 60%, 80%, 100%) for 1 h each at RT. Samples were then incubated overnight in 2/3 anhydrous dichloromethane anhydrous (DCM)–1/3 methanol solution. The next day, after 30 min incubation in 100% DCM, samples were transferred in 100% dibenzyl ether solution (DBE, Sigma-Aldrich, Steinheim, Germany). Cleared samples were imaged in DBE in specific 3D-printed chambers. Because DBE dissolves most materials, we sealed the 3D-printed chambers with a coverslide using Twinsil silicone glue (PicoDent, Wipperfürth, Germany), which does not react with DBE. Samples were imaged using an inverted microscope, DMi8 (Leica Microsystems, Wetzlar, Germany) equipped with a spinning disk head (Yokogawa CSU-W1), and a sCMOS ORCA-FLASH 4 V2+ camera (Hamamatsu, Hamamatsu City, Japan). Acquisitions were performed with MetaMorph (Molecular Devices, Sunnyvale, CA, USA) software. 3D-reconstructions and movies (Videos S7 and S8) were generated with Imaris (Bitplane) software.

Tuj and SMA immunostaining on transverse sections

Guts were fixed for 1 h in a 4% paraformaldehyde in PBS solution, washed in PBS, then left overnight in 30% sucrose in water solutions, and embedded the next day in OCT compound (VWR, Paris, France). Slices of 14 μm were cut at −20°C with a cryotome (Leica) and deposited on Thermofrost glass slides (VWR). After rehydration and blocking of the slides for 15 min in a 1% BSA in PBS solution, the slides were then incubated overnight in an anti-α smooth muscle actin antibody (Abcam, ref 5694, dilution 1:1000) and anti βIII-tubulin antibody (Abcam, ref 14545, dilution 1:1000) solution composed of 1% BSA and 0.1% Triton X-100 in PBS; the following day, after washing, complementary fluorescent secondary antibodies (CY3 and Alexa488, dilution 1:400 in PBS) were applied for 6 h. The slides were washed and immediately imaged with a confocal microscope.

Results

### Physiological motility characteristics from E12 to E16

Figures 2 and 3 provide, respectively, a qualitative and quantitative overview of the movements observed from stages E12–E16. At stage E12, motility consisted in circular smooth muscle contraction waves (CC waves) that propagated along the gut at constant velocity (Fig. 2*A* and Video S1). Contractions occurred spontaneously along the gut segment or at its extremities and gave rise to two counter-propagating waves traveling away from the origination site. When two oppositely propagating waves met, they annihilated. This behaviour is in all

aspects identical to what we described earlier for E6–E9 guts (Chevalier *et al.* 2017). CC waves did not exhibit any preferential rostro-caudal or caudo-rostral direction at any of the stages examined (E12–E16).

Longitudinal smooth muscle is known to differentiate in the chicken at E13 (Shyer *et al.* 2013). E14 (Video S1) and E16 (Videos S2–S5) duodenum and jejunum exhibited a periodic, low-frequency ($\sim$0.3 cpm) rocking motion in the transverse direction (*x*-axis in Fig. 1*B*), which was super-imposed with higher-frequency ($\sim$3 cpm) CC waves (Fig. 2*B–D*). The rocking motion was accompanied by a slight periodic increase in gut length ($\sim$5–10%). To identify the origin of this motion, we performed particle-image velocimetry (using the 'Tracker' ImageJ plugin, courtesy of O. Cardoso) on open gut preparations (Video S2 and Fig. 1*B*). Longitudinal contractions (LC, Fig. 2*E*, left) compressed the epithelium along the longitudinal direction and stretched it along the transverse direction at a frequency of $\sim$0.3 cpm. Conversely, circular contractions (CC, Fig. 2*E*, right) compressed the epithelium along the transverse direction and stretched it in the longitudinal direction, but at a higher frequency of $\sim$3 cpm. This confirms that the $\sim$0.3 cpm rocking motion we observe in tubular preparations is due to longitudinal contractions. The decrease in length during a LC was much more pronounced in open preparations because the gut could more freely expand in diameter than in a tubular

preparation. We did not detect longitudinal contractions in the hindgut in the period E12–E16.

At stage E16, duodenal segments exhibited a marked correlation between longitudinal bulk (whole-segment) contractions and circular contractions (Fig. 2*C* and Video S3): when longitudinal muscle was contracted ($d_s(t)$ peaks, see Fig. 2*C*), CC wave amplitude $A_c(t)$ significantly decreased or even vanished, i.e. these two signals were out of phase with one another. In $n = 10/67$ E16 duodenal segments, we detected localized diameter bulges (spanning $\sim$1 mm) that propagated along the length of the intestine (Video S4). These propagating bulges are distinctly seen on spatiotemporal maps (light, slanted streaks indicated with arrowheads in Fig. 2*D*). They had an average speed of 38 ± 7 μm/s ($n = 10$) and a frequency of $\sim$0.3 cpm. Circular contraction waves propagated towards or away from the bulge, but wave amplitude at the site of the bulge was zero. The diameter bulges were generated at the same frequency as bulk longitudinal contractions. They had the same inhibitory effect on circular wave amplitude as bulk longitudinal contractions. We therefore must conclude that the local propagating diameter bulge is due to a local, propagating, longitudinal contraction. In the following we will refer to this motion pattern as a migrating motor complex (MMC; Roberts *et al.* 2010). We found that in all samples where MMCs were present, they propagated in the rostro-caudal direction. The complexes therefore

Quantitative characteristics of motility
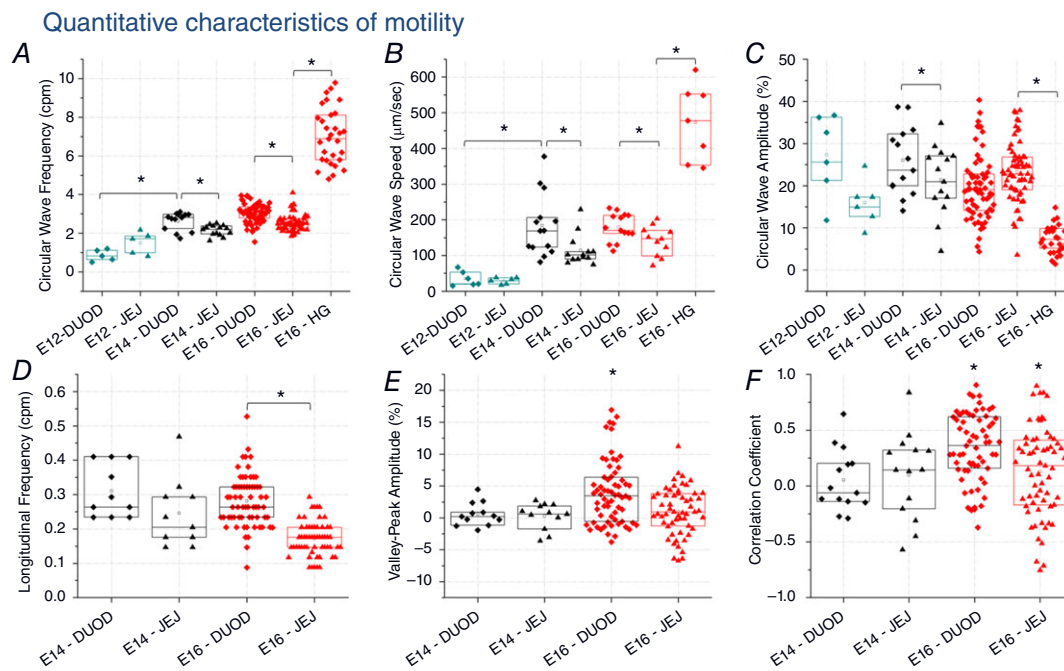
Figure 3. Quantitative characteristics of circular, longitudinal and circular–longitudinal coupling at E12–E16
Each data point corresponds to a different sample. A star indicates a statistically positive (>0) value, Student's *t* test $P < 0.05$. A star over a bracket indicates a statistically significant difference between groups ($P < 0.05$, Mann–Whitney two-tailed test).
[Colour figure can be viewed at wileyonlinelibrary.com]

represent the first motility pattern in the embryo with a preferential, aboral propagation direction. Figure 2*F* summarizes the movements observed in each segment of the lower gastrointestinal tract at stages E12–E16.

CC frequencies (Fig. 3*A*) and wave speeds (Fig. 3*B*) were significantly higher in the E16 duodenum (3.1 ± 0.2 cpm, $n = 65$, all uncertainties are $\pm$SD/2) than in the jejunum (2.5 ± 0.2 cpm, $n = 63$); a similar difference between duodenum and jejunum was present at E14 (Fig. 3*A* and *B*). Similarly, LC frequency (Fig. 3*D*) was significantly higher in the E16 duodenum (0.28 ± 0.04 cpm, $n = 65$) than in the jejunum (0.17 ± 0.02 cpm, $n = 57$). We measured a significant, abrupt, 4- to 5-fold increase of CC wave speed between E12 and E14 (Fig. 3*B*) from 35 ± 11 μm/s ($n = 6$) to 184 ± 42 μm/s ($n = 14$) in the duodenum, and from 29 ± 5 ($n = 6$) to 114 ± 22 μm/s ($n = 13$) in the jejunum. In the E16 hindgut, the frequency of CC waves (Fig. 3*A*) was 7.3 ± 0.8 cpm ($n = 22$), a factor $\sim$2 higher than in the midgut. The speed of CC waves (Fig. 3*B*) in the hindgut was in the range 200–600 μm/s, i.e. a factor $\sim$3 higher than in the midgut; 1 Hz time-lapse acquisition was actually not sufficient to accurately measure wave speed in the hindgut. CC wave amplitude (Fig. 3*C*) was $8.0 \pm 1.7\%$ ($n = 30$), i.e. a factor $\sim$3 lower than in the midgut. We quantified the correlation between bulk LC and local CC wave amplitude by computing two indicators: the Pearson correlation coefficient and the average difference of contraction amplitude at diameter valleys (minima) and diameter peaks (maxima), as described in the Methods. Figure 3*E* and *F* shows that both indicators are significantly >0 in E16 duodenum ($\rho = 0.34 \pm 0.15$, VP = $3.9 \pm 2.5\%$), whereas they are not significantly different from zero in all other preparations (E14 duodenum and jejunum and E16 jejunum).

Effects of drugs on tonic and phasic contractility

The effect of neuronal inhibitors and of the muscle agonist NO in the duodenum are presented in Fig. 4*A*–*H* and illustrated in Videos S3–S5.

We first used tetrodotoxin (TTX, 1 μM) to determine when smooth muscle contractions become dependent on the activity of the enteric nervous system. We found that TTX had no effect at E12 (Fig. 4*A*–*F*) showing that motility at this stage is purely myogenic, as we found for earlier stage guts (E7–E9; Chevalier *et al.* 2017). At E14, TTX caused a slight but significant diameter decrease (Fig. 4*A*) of $-2.8 \pm 0.8\%$ ($n = 12$); none of the other characteristics (Fig. 4*B*–*G*) examined were affected. The diameter decrease corresponded to an immediate constriction of the whole duodenum segment following drug addition, caused by the increase of circular smooth muscle tone. At stage E16, TTX induced a more pronounced diameter decrease of the duodenum of $-7.1 \pm 2.8\%$ ($n = 14$, Fig. 4*A* and Video S4). TTX

also caused a significant increase of CC wave amplitude by $13 \pm 8\%$ ($n = 14$, Fig. 4*B*). It finally induced a net decrease of the correlation coefficient (-0.25 ± 0.15, $n = 13$, Fig. 4*D*) and of the valley–peak indicator ($-2.6 \pm 1.9\%$, $n = 11$, Fig. 4*C*), showing that coupling between the longitudinal and circular muscle layers was reduced or abolished. We further found that, in all samples ($n = 3$) in which propagating contraction complexes were present before drug addition, this motion pattern was abolished by TTX (spatiotemporal map Fig. 4*H* and Video S4). TTX did not affect CC wave speed (Fig. 4*F*) or CC and LC frequency (Fig. 4*E* and *G*).

We applied atropine and NOLA to inhibit more specifically excitatory and inhibitory neuronal pathways at E16. Atropine (10 μM) did not have a significant effect on any of the quantities examined (Fig. 4*A*–*G*). Similarly to TTX, NOLA (100 μM) led to diameter decrease of $-2.7 \pm 1.9\%$ ($n = 26$, Fig. 4*A*) and a $21 \pm 19\%$ ($n = 26$, Fig. 4*B*) increase in CC wave amplitude (Video S3). Like TTX, it also induced a net decrease of the correlation coefficient (-0.2 ± 0.1, $n = 26$, Fig. 4*D*) and of the valley–peak indicator ($-2.8 \pm 2.4\%$, $n = 26$, Fig. 4*C*), showing a reduction of the coupling between LC and CC (Video S3). NOLA did not abolish propagating contraction complexes ($n = 6$) but the amplitude of the diameter bulges appeared reduced. Like TTX, NOLA did not affect CC wave speed (Fig. 4*F*) or CC and LC frequency (Fig. 4*E* and *G*).

Because TTX and NOLA induced significant responses in E16 duodenal segments, we finally examined the effect of the neuronal nitric oxide synthase (nNOS) neuro-transmitter NO. To this end, we added the NO donor sodium nitroprusside (SNP 100 μM, Video S5), resulting in a NO concentration of 65 nM (Bradley & Steinert, 2015). SNP led to a significant increase of diameter of $4.3 \pm 1.9\%$ ($n = 12$, Fig. 4*A*), and a strong reduction of CC amplitude by $-58 \pm 10\%$ ($n = 12$, Fig. 4*B*). Correlation indicators increased slightly after SNP (Fig. 4*C* and *D*), essentially because CC waves had decreased to such an extent immediately after SNP application that CC amplitude and diameter curves overlapped (i.e. were correlated). Overall, the effects of exogenous NO on diameter, CC amplitude and CC–LC correlation are the opposite of those obtained by blocking endogenous NO synthesis by either TTX or NOLA. SNP also led to a significant reduction of CC frequency ($-9.0 \pm 2.9\%$, Fig. 4*E*) and of LC frequency ($-33 \pm 13\%$, Fig. 4*G*); the reduction was especially pronounced immediately after SNP addition; frequency then gradually increased in the 30 min period following drug application (Video S5).
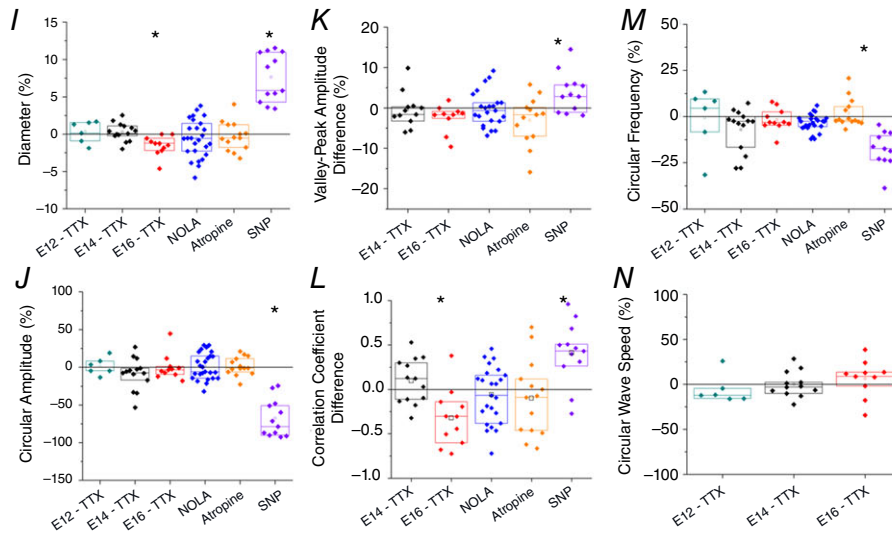
The effects of drugs on jejunal segments are summarized in Fig. 4*I*–*N*. E12 and E14 jejunal contractions were TTX-insensitive. The diameter reduction associated with TTX at E16 was small ($-1.7 \pm 0.7\%$, Fig. 4*I*) but significant. Unlike for duodenum, however, CC amplitude in the jejunum remained unchanged after TTX application
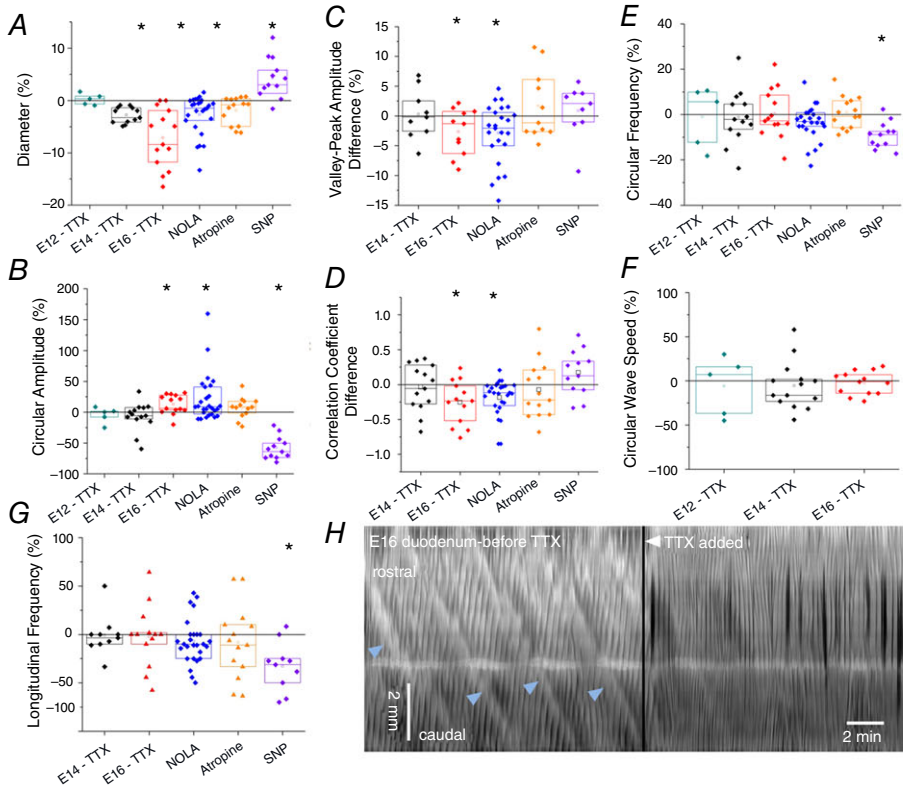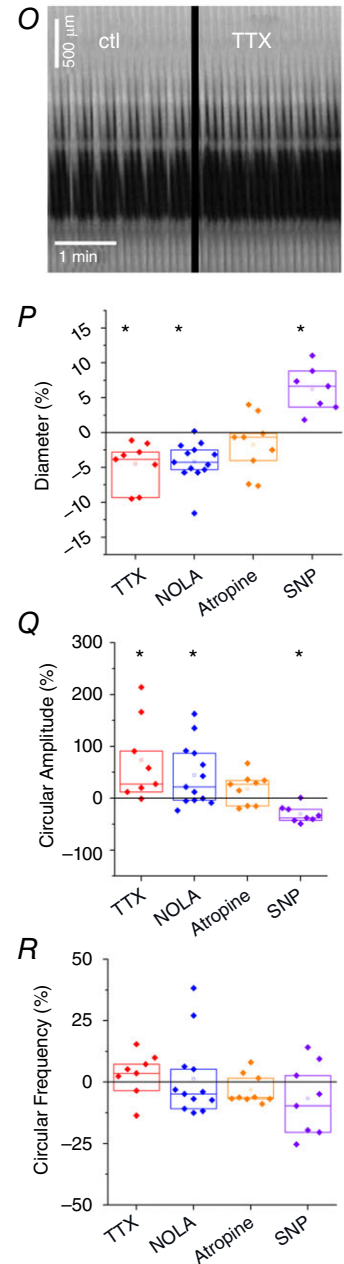
Figure 4. Effects of TTX, NOLA, atropine and sodium nitroprusside (SNP) in duodenum (*A–H*), jejunum (*I–N*) and hindgut (*O–R*)

Percent changes before-after drug addition are computed for any quantity q as $q = 100(q_{after} - q_{before})/q_{before}$. Because correlation indicators ρ and VP can be positive or negative, we computed their difference rather than their percent change, i.e. $\Delta\rho = \rho_{after} - \rho_{before}$ and $\Delta VP = VP_{after} - VP_{before}$. Each data point represents a different sample. A star indicates that a sample group is significantly different from zero, Student's *t* test, $P < 0.05$. The spatiotemporal map (*H*) illustrates that propagating contractile complexes (light slanted lines, arrowheads) in E16 duodenum vanish after application of TTX 1 μM. The spatiotemporal map (*O*) shows TTX-insensitive CC wave activity in the hindgut.
[Colour figure can be viewed at wileyonlinelibrary.com]

(Fig. 4*J*). Although TTX led to a decrease of the correlation coefficient (Fig. 4*L*), it did not yield a significant valley–peak difference (Fig. 4*K*), such that it cannot be said that CC–LC coupling is reduced by application of TTX in E16 jejunum. This conclusion is consistent with the fact that in the E16 jejunum, CC and LC are poorly correlated to start off with (in physiological conditions, Fig. 3*E*). Unlike in the duodenum, application of NOLA to jejunal segments did not have a significant effect on any of the quantities examined. Motility in the jejunum was insensitive to atropine, like in the duodenum. Overall, the effects of neuronal inhibitors (TTX, NOLA) in the E16 jejunum were much less pronounced than they were in the E16 duodenum. SNP induced essentially the same effects in the jejunum as it did in the duodenum (diameter increase, CC wave amplitude and frequency decrease).

In the E16 hindgut segments (Fig. 4*O*–*R*), TTX and NOLA caused a significant diameter reduction ($-4.6 \pm 1.6\%$, $n = 7$ and $-4.2 \pm 1.6\%$, $n = 9$, respectively, Fig. 4*P*), increased CC amplitude ($20 \pm 12\%$, $n = 7$ and $33 \pm 13\%$, $n = 9$, respectively, Fig. 4*Q*), while CC frequency was unaffected (Fig. 4*R*). Atropine did not have any effect on hindgut contractility. SNP caused a significant diameter increase ($6.6 \pm 1.9\%$, $n = 6$, Fig. 4*P*) and a significant reduction of CC amplitude ($-58 \pm 10\%$, $n = 6$, Fig. 4*Q*).

Response to mechanical stimulation

We previously demonstrated that early stage guts (E7–E9) are intrinsically mechanosensitive: when mechanical pressure is applied to the gut locally by pinching, it triggers two outgoing CC waves that propagate away from the point of compression (Chevalier, 2018). We investigate here the development of this reflex response on duodenal segments at the TTX-insensitive and TTX-sensitive stages E12 and E16, respectively. The response to pinching of E12 guts was identical to that of E7–E9 guts, i.e. it generated two outgoing CC waves (Fig. 5*A* and Video S6, $n = 6$ guts, $n > 20$ pinches). In some instances, a second or third pair of contractile waves was generated at the point of compression. This response was insensitive to tetrodotoxin (Fig. 5*A* bottom). Pinching at stage E16 led to a local, phasic, non-propagating contraction that lasted 10–30 s (see black oscillating spots at white arrows, Fig. 5*B*). Circular contraction waves were inhibited in a region spanning $\sim$1–2 mm rostral to the point of compression for 4–6 min (Fig. 5*B*, $n = 6$ guts, $n > 20$ pinches). CC waves on either side of the region of inhibition were still in register with each other (Fig. 5*B*, white connecting dashed lines), indicating that propagation of the signal associated with the contractile waves was not inhibited.

Pinching after TTX application (1 μM for 1 h, Fig. 5*B* bottom) triggered two outgoing CC waves, like for E12 guts; the wave that propagated in the direction opposite to that of the background contractile waves quickly annihilated; the wave that propagated in the same direction as the background waves fused with them in a way that the overall frequency of the contractile waves remained unchanged. Subsequent pairs ($\sim$5–10)
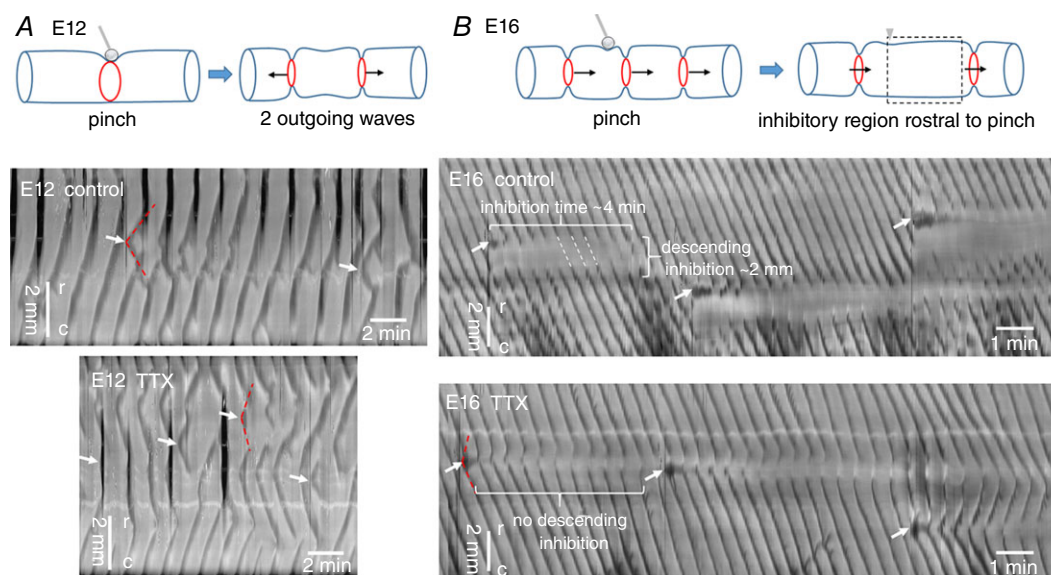
Figure 5. Response to local mechanical stimulation of duodenum at stage E12 (*A*) and E16 (*B*)
Top, schematic representation of physiological response to pinching. Bottom, spatiotemporal maps before (physiological) and after TTX application (1 μM for 1 h). Darker areas correspond to reduced gut diameter. White arrows indicate time and position of pinch (2–4 per map). Dashed lines at E12 indicate outgoing waves after pinching. White dashed lines at E16 show that circular waves are still in register on either side of the region of descending inhibition. r-c indicates the rostro-caudal direction (top-down in all spatiotemporal maps of this report).
[Colour figure can be viewed at wileyonlinelibrary.com]

of contractile waves were generated at the point of compression. The amplitude of CC waves at the point of compression was slightly reduced, but the region of descending inhibition observed prior to TTX application had vanished.

Gut clearing and 3D reconstitution of the enteric nervous system

We used the iDISCO+ clearing method with Tuj and DAPI immunohistochemistry on duodenum at the neural-control stage E16. Whole-mount tissue imaging is
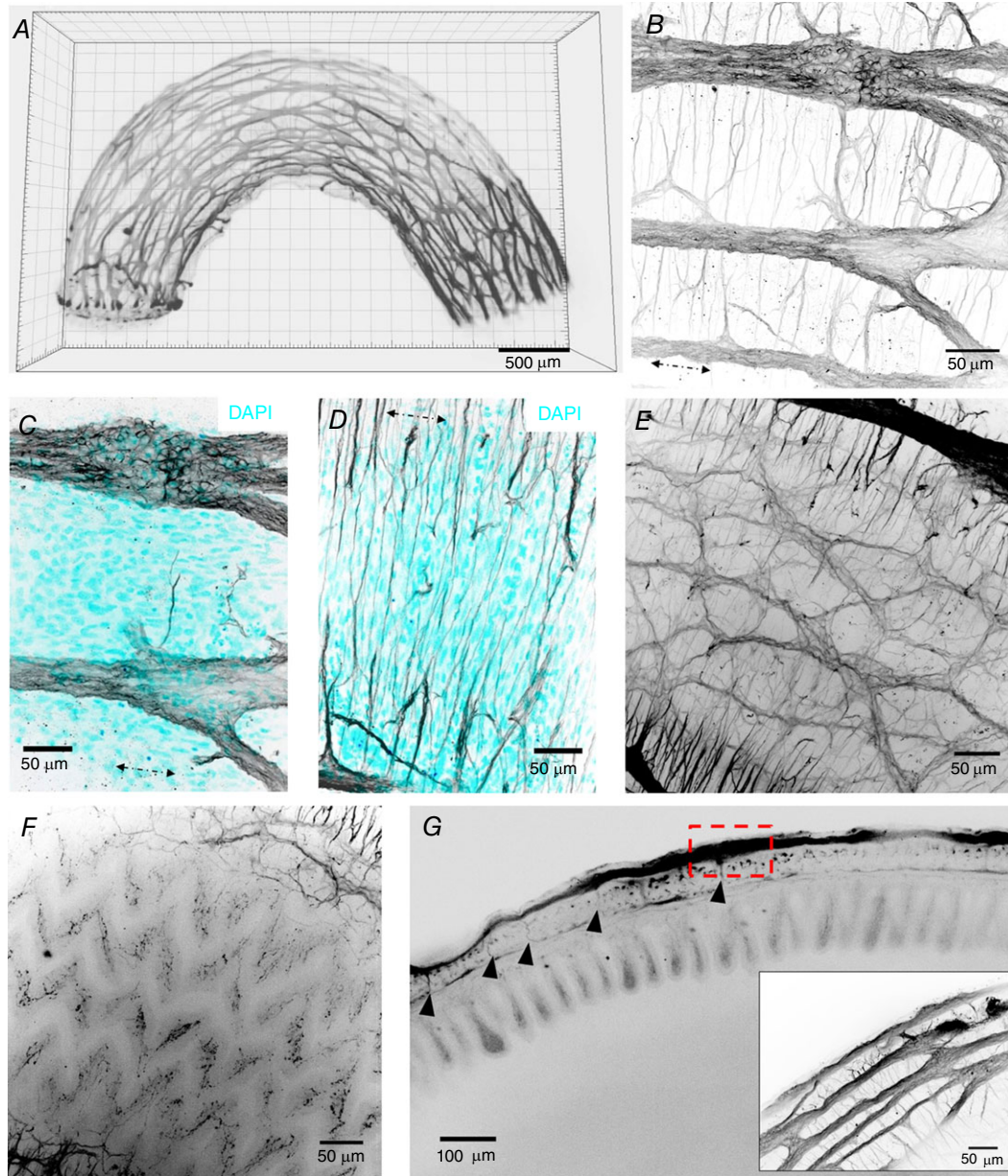
Figure 6. Enteric nervous system of E16 chicken duodenum revealed by confocal imaging of Tuj (βIII-tubulin) whole-mount immunohistochemistry on clarified tissue
A, still shot of 3D reconstruction (Video S7). *B–F*, still shots of Video S8. *B*, Z-stack max projection of myenteric plexus and circumferentially extending dendrites. *C*, Z-stack max projection of myenteric plexus showing enteric ganglia and longitudinally oriented cells (DAPI) belonging to the longitudinal smooth muscle layer. *D*, Z-stack max projection of circumferentially extending dendrites and circumferentially oriented cells (DAPI) belonging to the circular smooth muscle layer. *E*, submucosal plexus. *F*, dendritic projections of submucosal plexus in epithelial villi. *G*, longitudinal optical section showing neuromuscular coat, epithelial villi and lumen. Arrowheads: connections between the myenteric and submucous plexus. Inset: zoom of dashed region showing structure of myenteric ganglia at gut border.
[Colour figure can be viewed at wileyonlinelibrary.com]

usually limited to a depth of ∼100 µm by light scattering. Clearing techniques remove lipids, the main contributor to light scattering, and make the refractive index of the tissue homogeneous, thus drastically improving light penetration depth. In clarified tissues, the fluorescence signal could be retrieved throughout the ∼1 mm thickness of the segment, making it possible to reconstruct for the first time the 3D architecture of the chicken enteric nervous system (Fig. 6*A* and highly informative Video S7). We complemented 3D Tuj images with immuno-histochemistry on 2D transverse frozen sections to assess connectivity of enteric nerves to the smooth muscle (Fig. 7). The myenteric plexus is composed of 50–100 µm-wide ganglia interconnected by interganglionc fibres 10–30 µm in diameter (Fig. 6*A* and *B*). The fibres and ganglia form a polyhedral mesh that is elongated along the longitudinal axis of the gut. Nerve fibres extend circumferentially from myenteric ganglia to innervate the circular smooth muscle layer (Figs 6*B* and *D*, and 7). Interestingly, we did not observe a similar structure innervating the longitudinal muscle layer at this stage (Figs 6*B*, *C* and *G*, and 7): no dendrites were seen to extend longitudinally above or in the plane of the myenteric plexus. The submucosal plexus forms a looser mesh network below the circular muscle layer (Fig. 6*E*); the submucosal and myenteric plexus are connected by radial nerve fibres that penetrate between circular smooth muscle bundles (see optical longitudinal section Fig. 6*G*, arrowheads and Fig. 7). Dendrites from the submucosal plexus projected all the way to the tip of the epithelial villi (Figs 6*F* and *G*, and 7). Video S8 shows the progression inside the enteric nervous system from the myenteric plexus to the epithelium in a clarified tissue specimen.

Discussion

In this study we have described intestinal motility in the chicken fetus from stage E12 to E16. At E12, motility consists of myogenic circular smooth muscle contractions that propagate as waves along the intestine. Over-lapping and independent, myogenic, low-frequency, bulk longitudinal smooth muscle contractions then appear at E14. Tetrodotoxin-sensitive coupling of longitudinal and circular contractions by the enteric nervous system at E16 gives rise to a new directional, cyclical bolus transport pattern: the migrating motor complex.

We summarize in Table 1 important landmarks of the ontogenesis of motility in the chicken, human, mouse and zebrafish. From E5 to E12, the contractile activity of the chicken embryonic gut consists of CC waves that propagate along the gut tract (Chevalier *et al.* 2017). We have previously demonstrated by direct calcium imaging that spontaneously generated, intercellular, gap-junction-dependent circular smooth muscle calcium waves underpin this early motility pattern (Chevalier, 2018). Contractions at stage E5–E6 propagate rapidly (100–1000 µm/s), leading to apparent, immediate whole-gut contractions (Chevalier *et al.* 2017). They become localized and their speed decreases from E6 through E12; the speed then exhibits an abrupt, 5-fold increase between E12 and E14 (Fig. 3B). Under-standing this sudden speed increase will require further investigation. The amplitude and frequency of CC waves increase respectively from 0 to ∼25% and from ∼0.3 to ∼3 cpm between stages E6 and E14.

As development progresses, CC waves become more ordered: their rhythm becomes increasingly regular and successive waves tend to all propagate in the same direction for prolonged periods of time (compare spatio-temporal map of E7 gut in Chevalier *et al.* (2017) and of E12 and later guts in Fig. 2), although they do not, as a whole, exhibit a preferred rostro-caudal or caudo-rostral propagation direction. This progressive ordering of CC waves is probably the result of the activity of interstitial cells of Cajal (ICC), because firstly ICCs differentiate around E9 in the chicken gut (Lecoin *et al.* 1996) and secondly ICCs have been shown to be involved in regulating, ordering
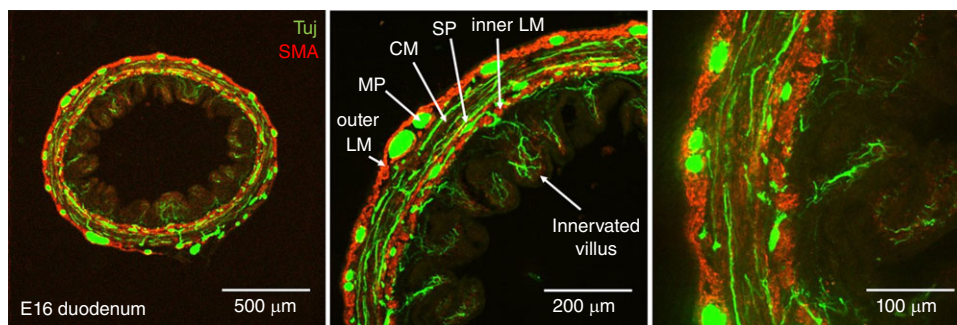
Figure 7. Enteric nervous system in relation to smooth musculature in 2D transverse section
Tuj and α-smooth muscle actin immunohistochemistry. CM, circular muscle; LM, longitudinal muscle; MP, myenteric plexus; SP, submucosal plexus. Circumferential Tuj-positive fibres extend in the circular smooth muscle layer and in the epithelial villi. At E16, an outer and an inner longitudinal muscle layer is present (Shyer *et al.* 2013).
[Colour figure can be viewed at wileyonlinelibrary.com]

Table 1. Summary of important landmarks in the emergence of gut motility in the chicken, human, mouse and zebrafish

Event	Chicken (days)	Human (weeks)	Mouse (days)	Zebrafish (days)
Enteric neural crest cell migration	4–8	4–8 (Wallace & Burns, 2005)	9.5–14.5	1–3 (Wallace *et al.* 2005)
First detectable nNOS neurons	—	14 (McCann *et al.* 2019)	11.5 (Hao & Young, 2009)	2 (Hao & Young, 2009)
Circular muscle differentiation	5–6 (Chevalier *et al.* 2017)	<7 (Beaulieu *et al.* 1993; Romanska *et al.* 1996)	12.5 (McHugh, 1995)	3 (Wallace *et al.* 2005)
Circular contractions	6,7 (Chevalier *et al.* 2017)	7.5 (Ueda *et al.* 2016), visible on MRI images	13.5 (Roberts *et al.* 2010)	4 (Holmberg *et al.* 2007)
Interstitial cell of Cajal differentiation	9 (Lecoin *et al.* 1996)	9 (Wallace & Burns, 2005)	14.5–18.5 (Roberts *et al.* 2010)	7 (Holmberg *et al.* 2007)
Longitudinal muscle differentiation	13 (Shyer *et al.* 2013)	12–14 (Wallace & Burns, 2005)	16 (Walton *et al.* 2016)	4–5 (Wallace *et al.* 2005)
Longitudinal contractions	14	—	—	—
Calcium activity in enteric neurons		16 (McCann *et al.* 2019) electrically evoked, TTX-sensitive	12.5 (Hao *et al.* 2017), not correlated with motor patterns	
Neurally mediated motility	16		16.5–18.5 (Roberts *et al.* 2010)	5–7 (Holmberg *et al.* 2007)

Calcium signals detected in the mouse by (Hao *et al.* 2017) do not seem to be related to motor patterns; calcium signals detected by (McCann *et al.* 2019) could be related to motor patterns as they are TTX-sensitive. Note that the order of events is the same in all four species. It is a remarkable fact that human and chick gut development follow the same timeline, in days for the chicken, in weeks for humans.

and entraining CC waves (Hennig *et al.* 2010). CC wave generation and propagation do not, however, require ICCs or neural activity, as they are TTX-insensitive (Figs 3 and 4) and are found in aganglionic chick hindgut (Chevalier *et al.* 2017), in aganglionic mouse mid- (Roberts *et al.* 2010) and hindgut (Roberts *et al.* 2008), and also in embryonic (Roberts *et al.* 2010) and adult (Hennig *et al.* 2010) W/W^V mouse guts lacking myenteric ICCs. Interestingly, ICC-depleted mice are viable although they present dilated intestines and disrupted motility patterns (Rich *et al.* 2013). This shows that even disordered CC waves can give rise to the coupled, neurogenic movements that emerge later in development and are essential for bolus transport and digestion.

Longitudinal smooth muscle differentiation is the next important milestone in the development of motility. It occurs at stage E13 in the chicken embryo (Shyer *et al.* 2013). Soon thereafter, at stage E14, we detected low-frequency (∼0.3 cpm) whole-segment LCs, superimposed on higher-frequency (∼3 cpm) CC waves. Pacing is believed to occur predominantly by ICC-MY interstitial cells of Cajal, located in or close to the myenteric plexus (Sanders *et al.* 2014). Studies in the canine colon (Smith *et al.* 1987) have shown that distinct ICC subnetworks can generate different pacemaker frequencies: a similar mechanism might be at play in the chicken to generate the 10-times lower frequency of LCs compared to CCs. It is also possible that the freshly differentiated longitudinal muscle layer at E14–E16 is not yet connected to ICCs. Just

like CCs, LCs persisted in the presence of TTX. LCs and CCs occur independently of one another at E14. Neural inhibition by tetrodotoxin (TTX) induces a slight but significant constriction of diameter in duodenum at stage E14 (Fig. 4*A*), a first sign of neural activity on smooth muscle contractility. Physiological neuronal activity at this stage relaxes circular smooth muscle; this relaxing effect is blocked upon TTX addition, leading to constriction. This contractile effect of TTX becomes more pronounced at E16, by increasing both circular muscle tone (diameter decrease, Fig. 4*A*) and phasic CC wave amplitude (Fig. 4*B*). A recent study on the emergence of electrical activity in the human colon showed that TTX-sensitive electrically evoked calcium transients in enteric neurons are detected by week 16 (McCann *et al.* 2019). It is a remarkable fact that human and chick gut development follows almost exactly the same timeline, in days for the chicken, in weeks for humans (Fig. 8*A*). As in zebrafish, mice and human, neural activity in the chicken ENS sets in right after longitudinal smooth muscle differentiation (Table 1).

Motility in stage E16 duodenum is characterized by the emergence of a coupling between LCs and CCs: we found that when longitudinal muscle is contracted, gut diameter increases and CC wave amplitude is significantly decreased or even abolished (Figs 2*C* and 3*E* and *F*). LC–CC coupling disappears in the presence of TTX (Fig. 4*C* and *D*), showing that the coupling is mediated by neurons. When longitudinal contraction occurs locally (in ∼15% of E16 duodenum samples examined), LC–CC

coupling gives rise to a caudally propagating diameter bulge, the migrating motor complex (Roberts *et al.* 2010). MMCs are the first rostro-caudally polarized motility patterns in the embryonic gut. The frequency of MMC generation is the same as that of LCs (~0.3 cpm); they propagate at speeds of ~40 μm/s; because MMCs are the result of local LC–CC coupling, they vanish in the presence of TTX in chicken (Fig. 4*H*) and in mice (Roberts *et al.* 2010). The signal associated with a CC wave can travel through an MMC (Figs 2*D* and 4*H*), but the amplitude of CC waves is zero at the site of the MMC, as though the circular muscle was locally anaesthetized.

Comparison of duodenal and jejunal segments at identical stages revealed a rostro-caudal maturation gradient: neurally controlled movements (TTX and NOLA-sensitive LC–CC coupling, MMCs) were present in E16 duodenum but not yet in the E16 jejunum (Fig. 2); both the speed and the frequency of CC waves and the frequency of LCs were higher in duodenum than in jejunum (Fig. 3*A*, *B* and *D*), a gradient that has been observed for over a century in adult guts (Alvarez, 1914). Similarly to TTX, inhibition of nNOS activity by NOLA induced an increase of circular muscle tone, of CC wave amplitude, and uncoupled LC and CC in E16 duodenum (Fig. 4 and Video S3). Applying the nNOS agonist NO had the opposite effect to those of TTX and NOLA on smooth muscle tonic and phasic contractility (Fig. 4 and Video S5). In the newly hatched chicken (i.e. only 4–5 days after E16), NOS, vasointestinal peptide (VIP) and NADPH-diaphorase positive neurons have been detected throughout the enteric nervous system (Balaskas *et al.* 1995); nerve fibres were concentrated in the circular smooth muscle layers, and very few, if any, fibres were detected in the longitudinal muscle.

These findings are consistent with the predominantly inhibitory and NOLA-sensitive activity of the ENS on circular muscle we report here. NOLA only diminished the amplitude of MMCs, without completely abolishing them like TTX. This may indicate a role for VIP in driving smooth muscle relaxation in the embryonic gut at these stages. nNOS neurons are the first neuron sub-type to differentiate in the murine ENS (Hao *et al.* 2013). In the human colon (McCann *et al.* 2019), excitatory neurons (vesicular aceytylcholine transporter and substance P) differentiate before inhibitory neurons (nNOS and VIP). Acetylcholinesterase staining (using the Acetyl-cholineesterase Rapid Staining Kit no. 8450, MBL, Nagoya, Japan) showed that cholinergic neurons are present in myenteric ganglia thoughout the chicken gut at E16 (data not shown but available upon request). They are not active, as blocking this pathway with atropine did not have any effect on gut motility.

Mechanically stimulating the guts (Fig. 5) revealed further crucial information. Pinching leads to local thinning and distension (~50% diameter increase) of the gut wall. Although this stimulation method does not yield a stress pattern identical to that obtained by applying fluid or solid pressure inside the lumen (bolus), it could be applied reproducibly with precision concerning both the location and duration of stimulation. We find that pinching at stage E12 leads to the generation of two contractile waves that propagate away from the point of compression. Pinching at stage E16 leads to a localized contraction, followed by the inhibition of CC waves over a distance of ~1–2 mm caudal to the point of compression, for ~5 min. An E12-like myogenic response was recovered after neuronal inhibition of E16 guts by tetrodotoxin. We therefore conclude that the ENS drives a transition from a

A   LC-CC coupling

B   MMC propagation
Reaction to pinching
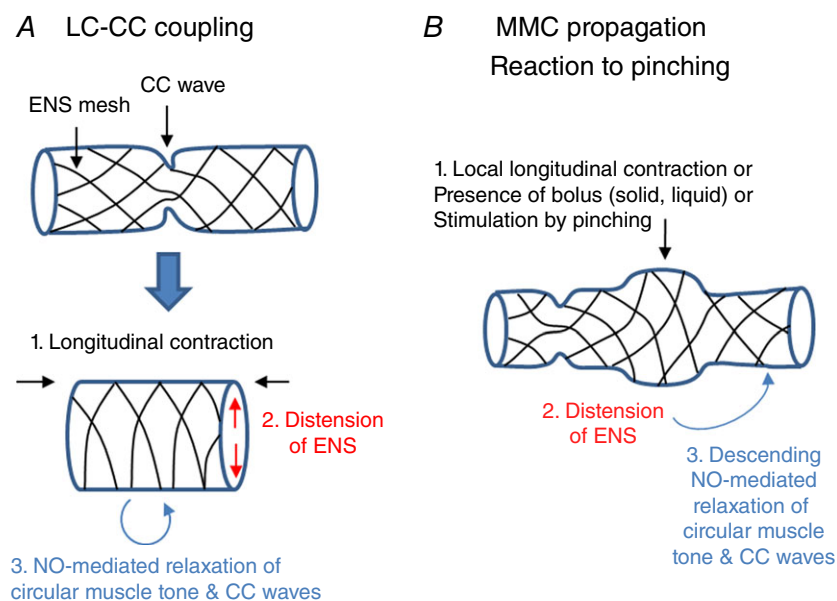
Figure 8. Schemes illustrating the suggested mechanosensitive mechanism for coupling of bulk longitudinal and circular contractions (*A*, LC–CC coupling) by the enteric nervous system, and its local version (*B*) responsible for propagation of the MMC and the observed reaction to mechanical stimulation (pinching) [Colour figure can be viewed at wileyonlinelibrary.com]

myogenic, symmetric reaction to mechanical stimulation at E12 to an asymmetric (polarized) reflex at E16 by actively inhibiting the caudally directed CC wave that is generated upon stimulation. The E16 reflex is very much alike the 'law of the intestine' (descending inhibition, ascending contraction) as first described by Bayliss and Starling (1899).

Our findings support the view that the ENS in the fetal chicken gut drives an active reciprocal coupling of longitudinal and circular smooth muscles (LC–CC coupling). We suggest that this neural coupling is mediated by the following mechanism (Fig. 8*A*): when longitudinal muscle is contracted, the resting diameter of the gut increases slightly due to passive mechanical cross-effects, putting the ENS under tension. Although this cross-deformation is small, it is potentially sufficient to activate mechanosensitive ENS neurons that amplify the effect by relaxing the circular smooth muscle by secretion of NO. Point mechanical stimulation of the embryonic gut (Fig. 5) suggests that a local, polarized version of the same mechanism (Fig. 8*B*) may explain the propagation of the MMC by the following steps: firstly a longitudinal contraction initiates a MMC by sucking liquid inside the gut lumen at its rostral end, secondly this liquid exerts pressure on the gut wall, distending the ENS and causing inhibition of CC waves caudal to the location of the bolus, while continuous CC waves maintain a small lumen size rostrally, and thirdly this asymmetry pushes the liquid bolus caudally, driving further caudal inhibition and a net, continuous rostro-caudal transport. This sequence of events is called the neuromechanical loop mechanism (Dinning *et al.* 2014). When the gut is pinched, the compressed region does not propagate (Fig. 5) because there is no liquid bolus. A prediction of this propagation model is that MMC velocity should depend upon the viscosity and physical characteristics of the bolus; this prediction has been verified for adult guts (Spencer *et al.* 2016).

We stress that the reciprocal coupling we observe cannot be accounted for solely by passive mechanical cross-effects because (1) LC–CC coupling and MMCs are sensitive to TTX, and thus actively mediated by the ENS (Fig. 4*C*, *D* and *H*), and (2) passive mechanical effects are relatively small and would yield a more graded correlation, whereas we observed that CC waves could completely disappear during a bulk longitudinal contraction (Video S3), and that CC amplitude was always zero at the site of a local longitudinal contraction (MMC, Video S4). Previous investigators have reported reciprocal motion of longitudinal and circular muscle (Kottegoda, 1969; Grider, 2003). This notion has been challenged by simultaneous electrophysiological recordings of longitudinal and circular smooth muscle layers showing that both layers receive synchronous excitatory nerve input oral to and synchronous inhibitory nerve input anal to the site of stimulation (Spencer *et al.* 1999, 2003; Spencer & Smith, 2001). In our study, longitudinal muscle does not appear to be innervated, as none of the neurotoxins tested had any effect on longitudinal contractions. The mechanism we suggest to explain the active LC–CC coupling and the MMC (Fig. 8) does not imply reciprocal hard wiring of longitudinal and circular muscle layers by the ENS, but does require passive mechanical interaction of the longitudinal layer with the ENS mesh in intact tubular preparations. It is possible that this mechanosensitive pathway may have been suppressed in preparations where this mechanical interaction was eliminated (Spencer *et al.* 1999). We also note that previous studies (Kottegoda, 1969; Spencer *et al.* 1999, 2003; Spencer & Smith, 2001; Grider, 2003) were all performed on adult, not embryonic guts, in the colon and ileum, not in the duodenum, and in guinea-pig or rat, not in the chicken. Differences in behaviour related to species and segment location cannot be excluded. We also expect further muscle innervation and neuronal subtype differentiation/activation to occur at later embryonic and postnatal stages, giving rise to different and more complex motor behaviour that the ones we report on within the scope of this study.

Tissue clarification made it possible to acquire fluorescence signal throughout the gut and to present a uniquely detailed optical 3D reconstruction of the beautiful enteric nerve meshwork (Fig. 6 and Videos S7 and S8). It revealed a dense network of circumferential neural projections from ganglia to the circular muscle layer (Figs 6*B* and *D*, and 7). This is consistent with the observed effects of neurotoxins (TTX, NOLA) on circular muscle contractility at this stage (Fig. 4). The slow outgrowth of these projections between E8 and E14–E16 likely explains the prolonged lapse of time between complete colonization of the gut by enteric crest cells (E8) and the first neural effects on motility (E16). We found that, at E16, the myenteric plexus is connected to the submucous plexus which in turn projects to the epithelial villi (Figs 6*F* and *G*, and 7). We did not, however, find a particular dendrite or neuronal projection structure innervating the longitudinal muscle layer at this stage.

In conclusion we have outlined the development of motility in the chicken embryo from stages E12 to E16, and examined the emergence of neurally controlled motility patterns in the context of longitudinal smooth muscle differentiation. Our investigation highlights that the 'engine' driving gut movements at this early stage of development is spontaneous myogenic contractile waves. Because these waves do not have a preferential rostro-caudal or caudo-rostral direction, they cannot efficiently propel luminal content. We found that the enteric nervous system orchestrates (Huizinga & Lammers, 2008) these spontaneous myogenic waves by inducing a polarized, caudal inhibition of circular

contraction waves upon distension of the gut wall. The distension can be triggered either by contraction of the longitudinal muscle layer or by local mechanical stimulation of the gut due to the presence of a bolus, or by external mechanical stimulation (pinching). This polarized mechanosensitive coupling of longitudinal and circular movements by the enteric nervous system generates a new directional, cyclical, propagating motility pattern that will efficiently transport the bolus in the adult: the migrating motor complex. Focusing on the simpler, embryonic rather than adult gut has allowed us to understand in detail and with a minimal number of *ad hoc* hypotheses the emergence of this new motility pattern.

References

Alvarez W (1914). Functional variations in contractions of different parts of the small intestine. *Am J Physiol* **35**, 177–193.

Balaskas C, Saffrey MJ & Burnstock G (1995). Distribution and colocalization of NADPH-diaphorase activity, nitric oxide synthase immunoreactivity, and VIP immunoreactivity in the newly hatched chicken gut. *Anat Rec* **243**, 10–18.

Barnes KJ, Beckett EA, Brookes SJ, Sia TC & Spencer NJ (2014). Control of intrinsic pacemaker frequency and velocity of colonic migrating motor complexes in mouse. *Front Neurosci* **8**, 96.

Bayliss WM & Starling EH (1899). The movements and innervation of the small intestine. *J Physiol* **24**, 99–143.

Beaulieu J, Jutras S, Durand J, Vachon PH & Perreault N (1993). Relationship between tenascin and t-smooth muscle actin expression in the developing human small intestinal mucosa. *Anat Embryol* **188**, 149–158.

Belle M, Godefroy D, Couly G, Malone SA, Collier F, Giacobini P & Chédotal A (2017). Tridimensional visualization and analysis of early human development. *Cell* **196**, 161–173.

Bradley SA & Steinert JR (2015). Characterisation and comparison of temporal release profiles of nitric oxide generating donors. *J Neurosci Methods* **245**, 116–124.

Chevalier NR (2018). The first digestive movements in the embryo are mediated by mechanosensitive smooth muscle calcium waves. *Philos Trans R Soc B Biol Sci* **373**, 20170322.

Chevalier NR, Fleury V, Dufour S, Proux-Gillardeaux V & Asnacios A (2017). Emergence and development of gut motility in the chicken embryo. *PLoS One* **12**, e0172511.

Daniel EE, Collins SM, Fox JET & Huizinga JD (1989). Pharmacology of drugs acting on gastrointestinal motility. *Handbook of Physiology, Section 6, The Gastrointestinal System, Vol. 1, Motility and Circulation*, ed. Schultz SG & Wood JD, pp. 715–757. Oxford University Press, New York.

Dinning PG, Wiklendt L, Omari T, Arkwright JW, Spencer NJ, Brookes SJH & Costa M (2014). Neural mechanisms of peristalsis in the isolated rabbit distal colon: A neuromechanical loop hypothesis. *Front Neurosci* **8**, 75.

Grider JR (2003). Reciprocal activity of longitudinal and circular muscle during intestinal peristaltic reflex. *Am J Physiol Gastrointest Liver Physiol* **284**, G768–G775.

Hao MM, Bergner AJ, Hirst CS, Stamp LA, Casagranda F, Bornstein JC, Boesmans W, Vanden Berghe P & Young HM (2017). Spontaneous calcium waves in the developing enteric nervous system. *Dev Biol* **428**, 74–87.

Hao MM, Bornstein JC, Vanden Berghe P, Lomax AE, Young HM & Foong JPP (2013). The emergence of neural activity and its role in the development of the enteric nervous system. *Dev Biol* **382**, 365–374.

Hao MM & Young HM (2009). Development of enteric neuron diversity. *J Cell Mol Med* **13**, 1193–1210.

Hennig GW, Spencer NJ, Jokela-Willis S, Bayguinov PO, Lee HT, Ritchie LA, Ward SM, Smith TK & Sanders KM (2010). ICC-MY coordinate smooth muscle electrical and mechanical activity in the murine small intestine. *Neurogastroenterol Motil* **22**, e138-e151.

Holmberg A, Olsson C & Hennig GW (2007). TTX-sensitive and TTX-insensitive control of spontaneous gut motility in the developing zebrafish (*Danio rerio*) larvae. *J Exp Biol* **210**, 1084–1091.

Hu H & Spencer N (2018). Enteric nervous system structure and neurochemistry related to function and neuropathology. In *Physiology of the Gastrointestinal Tract*, 6th edn, ed. Said HM, pp. 337–356. Academic Press/Elsevier.

Huizinga JD & Lammers WJEP (2008). Gut peristalsis is governed by a multitude of cooperating mechanisms. *Am J Physiol Gastrointest Liver Physiol* **296**, G1–G8.

Kottegoda S (1969). An analysis of possible nervous mechanisms involved in the peristaltic reflex. *J Physiol* **200**, 687–712.

Lecoin L, Gabella G & Le Douarin N (1996). Origin of the c-kit-positive interstitial cells in the avian bowel. *Development* **122**, 725–733.

Lentle RG & Hulls CM (2018). Quantifying patterns of smooth muscle motility in the gut and other organs with new techniques of video spatiotemporal mapping. *Front Physiol* **9**, 338.

McCann CJ, Alves MM, Brosens E, Natarajan D, Perin S, Chapman C, Hofstra RM, Burns AJ & Thapar N (2019). Neuronal development and onset of electrical activity in the human enteric nervous system. *Gastroenterology* **156**, 1483–1495.e6.

McConalogue K & Furness J (1994). Gastrointestinal neurotransmitters. *Baillieres Clin Endocrinol Metab* **8**, 51–76.

McHugh KM (1995). Molecular analysis of smooth muscle development in the mouse. *Dev Dyn* **204**, 278–290.

Renier N, Adams EL, Kirst C, Wu Z, Azevedo R, Kohl J, Autry AE, Kadiri L, Umadevi Venkataraju K, Zhou Y, Wang VX, Tang CY, Olsen O, Dulac C, Osten P & Tessier-Lavigne M (2016). Mapping of brain activity by automated volume analysis of immediate early genes. *Cell* **165**, 1789–1802.

Rich A, Gordon S, Brown C, Gibbons SJ, Schaefer K, Hennig G & Farrugia G (2013). Kit signaling is required for development of coordinated motility patterns in zebrafish gastrointestinal tract. *Zebrafish* **10**, 154–160.

Ro S, Hwang SJ, Muto M, Jewett WK & Spencer NJ (2006). Anatomic modifications in the enteric nervous system of piebald mice and physiological consequences to colonic motor activity. *Am J Physiol Gastrointest Liver Physiol* **290**, G710–G718.

Roberts RR, Bornstein JC, Bergner AJ & Young HM (2008). Disturbances of colonic motility in mouse models of Hirschsprung's disease. *Am J Physiol Gastrointest Liver Physiol* **294**, G996–G1008.

Roberts RR, Ellis M, Gwynne RM, Bergner AJ, Lewis MD, Beckett EA, Bornstein JC & Young HM (2010). The first intestinal motility patterns in fetal mice are not mediated by neurons or interstitial cells of Cajal. *J Physiol* **588**, 1153–1169.

Romanska H, Moscoso G, Polak H & Draeger A (1996). Smooth muscle differentiation during human intestinal development. *Eur J Transl Myol* **6**, 13–19.

Sanders KM, Ward SM & Koh SD (2014). Interstitial cells: regulators of smooth muscle function. *Physiol Rev* **94**, 859–907.

Shyer AE, Tallinen T, Nerurkar NL, Wei Z, Gil ES, Kaplan DL, Tabin CJ & Mahadevan L (2013). Villification: how the gut gets its villi. *Science* **342**, 212–218.

Smith T, Reed J & Sanders K (1987). Interaction of two electrical pacemakers in muscularis of canine proximal colon. *Am J Physiol* **252**, C290–C299.

Spencer N, Walsh M & Smith TK (1999). Does the guinea-pig ileum obey the 'law of the intestine'? *J Physiol* **517**, 889–898.

Spencer NJ, Bayguinov P, Hennig GW, Park KJ, Lee H-T, Sanders KM & Smith TK (2007). Activation of neural circuitry and Ca^{2+} waves in longitudinal and circular muscle during CMMCs and the consequences of rectal aganglionosis in mice. *Am J Physiol Gastrointest Liver Physiol* **292**, G546–G555.

Spencer NJ, Dinning PG, Brookes SJ & Costa M (2016). Insights into the mechanisms underlying colonic motor patterns. *J Physiol* **594**, 4099–4116.

Spencer NJ, Hennig GW & Smith TK (2003). Stretch-activated neuronal pathways to longitudinal and circular muscle in guinea pig distal colon. *Am J Physiol Gastrointest Liver Physiol* **284**, G231–G241.

Spencer NJ & Smith TK (2001). Simultaneous intracellular recordings from longitudinal and circular muscle during the peristaltic reflex in guinea-pig distal colon. *J Physio* **533**, 787–799.

Stevens RJ, Publicover NG & Smith TK (2000). Propagation and neural regulation of calcium waves in longitudinal and circular muscle layers of guinea pig small intestine. *Gastroenterology* **118**, 892–904.

Ueda Y, Yamada S, Uwabe C, Kose K & Takakuwa T (2016). Intestinal rotation and physiological umbilical herniation during the embryonic period. *Anat Rec* **299**, 197–206.

Wallace AS & Burns AJ (2005). Development of the enteric nervous system, smooth muscle and interstitial cells of Cajal in the human gastrointestinal tract. *Cell Tissue Res* **319**, 367–382.

Wallace KN, Akhter S, Smith EM, Lorent K & Pack M (2005). Intestinal growth and differentiation in zebrafish. *Mech Dev* **122**, 157–173.

Walton KD, Whidden M, Kolterud A, Shoffner SK, Czerwinski MJ, Kushwaha J, Parmar N, Chandhrasekhar D, Freddo AM, Schnell S & Gumucio DL (2016). Villification in the mouse: Bmp signals control intestinal villus patterning. *Development* **143**, 427–436.

Additional information

Competing interests

The authors have no competing interests.

Author contributions

Experiments were performed at Laboratoire Matière Systèmes Complexe and confocal imaging at Institut Jacques Monod/Imagoseine. N.R.C. designed the work, acquired and analysed data and wrote the manuscript. N.D., C.J., L.L., C.G. and O.F. acquired and analysed data and critically revised the manuscript for important intellectual content. All authors approved the final version of the manuscript. All authors agree to be accountable for all aspects of the work in ensuring that questions related to the accuracy or integrity of any part of the work are appropriately investigated and resolved. All persons designated as authors qualify for authorship, and all those who qualify for authorship are listed

Funding

Acknowledgements

Supporting information

Additional supporting information may be found online in the Supporting Information section at the end of the article.

Video S1. Motility at E12 and emergence of longitudinal movements at E14.

Video S2. E16 duodenum, open preparations, showing distinct circular and longitudinal contractions.

Video S3. E16 duodenum, coupled longitudinal-circular movements and effect of NOLA 100 μM.

Video S4. E16 duodenum, migrating motor complex and effect of tetrodotoxin 1 μM.

Video S5. Effect of sodium nitroprusside 100 μM, E16 ileum.

Video S6. Reaction to point mechanical stimulation, E12 and E16.

Video S7. 3D reconstruction of the enteric nervous system, Tuj and DAPI, iDISCO cleared tissue, E16 duodenum.

Video S8. Z-stack of enteric nervous system, Tuj labeling, iDISCO cleared tissue, E16 duodenum.